
In Pursuit of CFD-based Wind Tunnel Calibrations

Jan-Renéé Carlson*
NASA Langley Research Center,
Hampton, VA 23681, USA

Computational fluid dynamic simulations of models tested in wind tunnels require a high level of fidelity and accuracy, particularly for the purposes of CFD validation efforts. Considerable effort is required to ensure a sufficient characterization of both the physical geometry of the wind tunnel, the thermodynamics of the tunnel, and flow conditions in the test section. The condition setting process among subsonic wind tunnels, with either a closed or an open throat, is generally the same, though they can differ in specific details of the thermodynamics. The derivation, application, and error estimation of condition setting and calibration is discussed. Computational flow solutions of the high-speed leg of the NASA Langley Research Center 14-by 22-Foot Subsonic Tunnel are used to evaluate the calibration process and assess calibration curve sensitivities. Duplicating the characteristics of a particular wind tunnel is difficult at best. A calibration curve derived from the computational method is demonstrated to be the most consistent method to use for tunnel condition setting.

Nomenclature

Roman letters

A	area
a	speed of sound
C'	14x22 facility calibration function
C' _k	specific kinetic energy method calibration function
C' _p	incompressible method calibration function
c _p	specific heat at constant pressure
F _{loss}	arbitrary loss coefficient
h	specific enthalpy
K	designates an unknown multiplication factor
K _{pr}	pitot loss coefficient, 0.998
M	Mach number
p	pressure
q	dynamic pressure
R	gas constant
Re	Reynolds number
T	temperature
V	velocity magnitude
x	streamwise Cartesian directions

Subscripts

i	incompressible
local	relating to a particular tunnel station
ref	reference condition
t	total conditions
vapor	vapor pressure
∞	freestream condition

Conventions

CFD	computational fluid dynamics
EC	entrance cone

*Research Scientist, Computational Aerosciences Branch, Associate Fellow AIAA.

RH	relative humidity
Sta.	tunnel station
SC	settling chamber
TS	test section

Symbols

γ	ratio of specific heats, (1.4 for air)
μ	bulk viscosity
ρ	density

I. Introduction

INITIALLY part of the NASA Junction Flow (JF) experiment [1, 2], the use of computational fluid dynamics (CFD) for modeling the flow in many NASA testing facilities is on-going. Understanding and improving modeling of the Langley Research Center 14- by 22-Foot Subsonic Tunnel (14 × 22) has been a major part of that effort. In the report by Rumsey et al. [3], inviscid and viscous calculations were performed on grids modeling the empty tunnel, and viscous calculations were performed using grids with the JF test article placed in the test section. For the empty tunnel simulations, the importance of highly accurate (as built) geometric descriptions was emphasized.

Along with the importance of using a faithful representation of the test section geometry, and to some degree the overall tunnel shape, the setting of boundary conditions was discussed as an equally critical aspect of the computations. Rogers et al. [4] also brought this issue up and developed a calibration formula to more closely align the conditions in the CFD with the conditions in the wind tunnel. That approach was carried one step further where the software for computing facility flow conditions was internally coupled with the CFD, allowing for both automated and manual methods to be used [3, 5, 6].

This paper examines the tunnel calibration process, comparing results between two thermodynamic equation assumptions and the physical facility. Computational solutions of the flow in the high-speed leg of the 14x22 are discussed. Calibration curves are calculated for several tunnel calibration and flow scenarios. The influence of flow survey locations on the calibration curves are discussed.

II. Survey of Subsonic Tunnel Calibration and Condition Equations

In order to make an acceptably accurate statement about the flow in the test section, the thermodynamic state of the tunnel must be measured in a sufficiently unbiased and consistent fashion so as to arrive at the same flow condition regardless of the contents of the test section, i.e., with or without a test article installed. Calibration and condition setting equations can vary depending on the tunnel design, flow speed, pressure, temperature, and medium. The calibration curves in subsonic, atmospheric tunnels like the 14x22, can vary with the test section geometry, e.g., closed vs. open throat, and flow conditioning, e.g., with and without boundary layer suction at the start of the test section. The following subsections review the background of two tunnel condition and calibration equation methodologies; one starting from incompressible flow assumptions and one starting from compressible flow assumptions, that can be applied to closed throat, subsonic tunnel configurations.

A. Incompressible Pressure-Based Theory

A notional sketch of the high-speed section of a wind tunnel, excluding the diffuser, is shown in Fig. 1. Three locations are noted in Fig. 3.29 in "Low-Speed Wind Tunnel Testing" by Pope[7], for gathering information concerning the flow in the tunnel. The nomenclature in this discussion will use SC (settling chamber), EC (entrance cone), and TS (test section) for L , S , and J , respectively, that are used in Pope's book. The starting point for both calibration theories discussed here is the Euler dynamic equation shown in Eq. 1.

$$\frac{1}{\rho} dp + \frac{1}{V} dV = 0 \quad (1)$$

Assuming an isothermal process and integrate over the interval from SC to EC in Eq 1.

$$\int_{SC}^{EC} \left(\frac{1}{\rho} dp + \frac{1}{V} dV \right) = \frac{1}{\rho_i} (p_{EC} - p_{SC}) + \frac{1}{2} (V_{EC}^2 - V_{SC}^2) = 0 \quad (2)$$

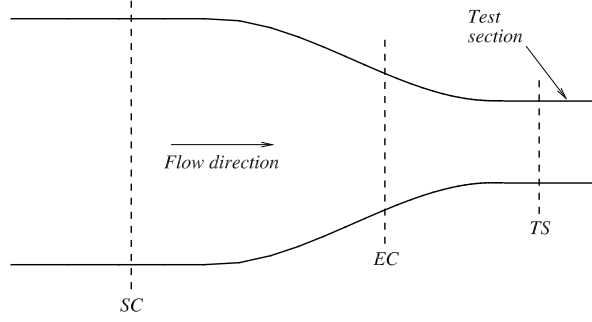


Fig. 1 Schematic of the two-point method, (taken from Pope [7], Fig. 3.29).

After rearranging the terms, the result is the familiar incompressible Bernoulli equation relating the pressure, p , and incompressible dynamic pressure, q_i . Additional aspects of incompressible flow are that the speed of sound is indeterminate and the Mach number equal to zero.

$$p_{SC} + q_{i,SC} = p_{EC} + q_{i,EC}, \quad \text{where } q_i = \frac{1}{2}\rho_i V^2 \quad (3)$$

An estimation of the incompressible dynamic pressure in the test section can be made using upstream flow information at SC and EC combined with the incompressible Bernoulli and continuity equations, Eqs. 4 and 5, respectively. The term $\mathcal{F}_{\text{loss}} q_{i,EC}$ represents some small energy loss between SC and EC.

$$p_{SC} + q_{i,SC} = p_{EC} + q_{i,EC} - \mathcal{F}_{\text{loss}} q_{i,EC} \quad (4)$$

$$(VA)_{SC} = (VA)_{EC} = (VA)_{TS} \quad (5)$$

The first point, at SC, measures the pressure of the tunnel flow in the large settling chamber and the second point, at EC, measures the pressure at some point upstream of the test section. The expectation, and primary assumption, is that the flow survey at EC is not significantly influenced by the presence of a model in the test section at TS.* The density terms in the continuity equation are constants due to the incompressible flow assumption and so drop out in these equations. The continuity equation, Eq. 5, is used to derive expressions for the dynamic pressures SC and EC.

$$q_{i,SC} = q_{i,EC} \left(\frac{A_{EC}}{A_{SC}} \right)^2, \quad q_{i,EC} = q_{i,TS} \left(\frac{A_{TS}}{A_{EC}} \right)^2 \quad (6)$$

$$p_{SC} = p_{EC} + \underbrace{\left(1 - \mathcal{F}_{\text{loss}} - \left(\frac{A_{EC}}{A_{TS}} \right)^2 \right) \left(\frac{A_{TS}}{A_{EC}} \right)^2}_{1/C'_p} q_{i,TS} \quad \left. \right\} \Rightarrow q_{i,TS} = C'_p (p_{SC} - p_{EC}) \quad (7)$$

Substituting Eq. 6 into Eq. 4 and after some manipulation, the change in the static pressure from the settling chamber to the entrance cone can be related to the dynamic pressure at a point in the test section, as shown in Eq. 7. The pressure difference, $p_{SC} - p_{EC}$, known as the indicated pressure, works quite well since differential measurements can typically be made more accurately than the process of measuring the absolute values of each pressure independently and then subtracting. The indicated pressure is adjusted per the tunnel calibration and is used to calculate a pressure, velocity and Mach number to be associated with the conditions in the test section.

In the chapter on tunnel calibrations in the first edition of Pope [7], the argument is made that if the inflow Mach number at SC is low enough, the pressure ratio, p/p_i , is very close to unity. Pope then substitutes the total pressure for the static pressure in the settling chamber as shown in Eq. 8. Assuming isentropic flow, for the range of Mach numbers

*Each facility and calibration process could guide the choice of EC and decide what may constitute a significant degree of influence.

- $M_L < 0.05$, the pressure ratio is $0.9983 \approx p/p_t$, and the total pressure is within 0.2% of the static pressure. This argument does not preclude using the static pressure in the settling chamber.

$$q_{i,TS} = C'_p (P_{t,SC} - P_{EC}) = C'_p q_{i,indicated} \quad (8)$$

With a pitot probe placed in the empty test section to measure the conditions at TS, the calibration equation can then be written as Eq. 9. The indicated incompressible dynamic pressure of the tunnel, $q_{i,indicated}$, is the difference in the pressures between locations SC and EC and the test section incompressible dynamic pressure, $q_{i,TS}$, is the pressure difference measured by the pitot probe at TS.

$$C'_p = \frac{q_{i,TS}}{q_{i,indicated}}, \text{ where } q_{i,TS} = P_{t,TS} - P_{TS} \quad (9)$$

The condition setting equations are summarized in Eqs.10 through 15. The incompressible dynamic pressure, $q_{i,TS}$, is calculated using the calibration function, C'_p , and the upstream pressure difference, also known as the indicated pressure, $q_{i,indicated}$, shown in Eq. 8. The incompressible Bernoulli equation is used to determine the static pressure at TS from the total pressure, $P_{t,SC}$, and the incompressible dynamic pressure, $q_{i,TS}$. Assuming isentropic, ideal gas relations, compressibility corrections are used to calculate the tunnel parameters, Mach number, M_{TS} , the compressible dynamic pressure, q_{TS} , and the density in the test section, ρ_{TS} . The equation for the dynamic pressure is used then to calculate the velocity in the test section, V_{TS} .[†]

$$q_{i,TS} = C'_p q_{i,indicated} \quad (10)$$

$$P_{TS} = P_{t,SC} - q_{i,TS} \quad (11)$$

$$M_{TS} = \left[\frac{2}{\gamma - 1} \left(\left(\frac{P_{t,SC}}{P_{TS}} \right)^{\frac{\gamma-1}{\gamma}} - 1 \right) \right]^{1/2} \quad (12)$$

$$q_{TS} = \frac{1}{2} \gamma P_{TS} M_{TS}^2 \quad (13)$$

$$\rho_{TS} = \rho_{t,SC} \left(\frac{P_{t,SC}}{P_{TS}} \right)^{-1/\gamma}, \text{ where } \rho_{t,SC} = \frac{P_{t,SC}}{R T_{t,SC}} \quad (14)$$

$$V_{TS} = \sqrt{2 q_{TS} / \rho_{TS}} \quad (15)$$

B. Compressible Enthalpy-Based Theory: Specific kinetic energy

This section will propose an alternate method for calibration assuming isentropic, compressible flow, rather than using the isothermal, incompressible flow assumptions discussed in Sec. II.A. The same starting point is used here with the dynamic equation previously shown in Eq. 1. Assuming an isentropic process, $p/\rho^\gamma \equiv \text{constant}$, and integrating over the interval from SC to EC results in the relationship shown in Eq 17.

$$\int_{SC}^{EC} \left(\frac{1}{\rho} dp + \frac{1}{V} dV \right) = \frac{P_t^{1/\gamma}}{\rho_t} \int_{SC}^{EC} p^{-1/\gamma} dp + \int_{SC}^{EC} \frac{1}{V} dV \quad (16)$$

$$= \frac{\gamma}{\gamma - 1} \left(\frac{P_{EC}}{\rho_{EC}} - \frac{P_{SC}}{\rho_{SC}} \right) + \frac{1}{2} (V_{EC}^2 - V_{SC}^2) \quad (17)$$

If the flow velocity at SC is brought isentropically to zero and the velocity and pressure at EC are taken as V and p , then Eq. 17 is just an expression of the compressible Bernoulli equation, more often written as in Eq.18.

$$\frac{\gamma}{\gamma - 1} \frac{p}{\rho} + \frac{1}{2} V^2 = \frac{\gamma}{\gamma - 1} \frac{P_t}{\rho_t} \quad (18)$$

[†]This derivation assumes that the total conditions in the test section are equal to the total conditions measured in the upstream settling chamber. Additionally, any transverse variation of the total pressure in the settling chamber, for example, would not be captured by single probe measurements.

Using the definitions, the specific enthalpy, h , and specific kinetic energy, k , the equation can be written as Eq.19.

$$h + k = h_t, \quad \text{where } h = \frac{\gamma}{\gamma - 1} \frac{p}{\rho} \quad \text{and } k = \frac{1}{2} V^2 \quad (19)$$

Using the same notional sketch, Fig. 1, the tunnel calibration problem is cast starting from the compressible specific kinetic energy equation rather than the incompressible, Bernoulli equation. An estimation of the kinetic energy in the test section is made by extrapolating the specific enthalpy from two upstream points, SC and EC. The specific enthalpy and a compressible form of the continuity equations are shown in Eqs. 20 and 21, respectively: essentially the same starting point used for developing the incompressible theory just discussed. The term $\mathcal{F}_{\text{loss}} k_{\text{EC}}$ represents some small amount of energy loss between the two stations.

$$h_{\text{SC}} + k_{\text{SC}} = h_{\text{EC}} + k_{\text{EC}} - \mathcal{F}_{\text{loss}} k_{\text{EC}} \quad (20)$$

$$(\rho VA)_{\text{SC}} = (\rho VA)_{\text{EC}} = (\rho VA)_{\text{TS}} \quad (21)$$

Using the compressible continuity equation, Eq. 21, to relate the specific kinetic energy at EC with the specific kinetic energy at TS, shown in Eq. 22, and the equation for total enthalpy, $h_{t,\text{SC}} = h_{\text{SC}} + k_{\text{SC}}$, into the enthalpy balance, Eq. 20, the extrapolation equation can be written as Eq. 23. The parameters in front of the k_{TS} term are grouped together and represented by the inverse of the calibration function C'_k .

$$k_{\text{EC}} = \left(\frac{\rho_{\text{TS}}}{\rho_{\text{EC}}} \right)^2 \left(\frac{A_{\text{EC}}}{A_{\text{TS}}} \right)^2 k_{\text{TS}} \quad (22)$$

$$h_{t,\text{SC}} = h_{\text{EC}} + \underbrace{(1 - \mathcal{K}) \left(\frac{\rho_{\text{TS}}}{\rho_{\text{EC}}} \right)^2 \left(\frac{A_{\text{EC}}}{A_{\text{TS}}} \right)^2 k_{\text{TS}}}_{1/C'_k} \implies k_{\text{TS}} = C'_k (h_{t,\text{SC}} - h_{\text{EC}}) \quad (23)$$

The calibration equation, in this case, is the measured specific kinetic energy in the test section divided by the enthalpy change between stations SC and EC shown in Eq. 24.

$$C'_k = \frac{k_{\text{TS}}}{h_{t,\text{SC}} - h_{\text{EC}}} \quad (24)$$

Assuming the flow is calorically and thermally perfect, the specific enthalpy can be expressed as $h = c_p T$; such that Eq. 24 can be written as Eq. 25.

$$C'_k = \frac{T_{t,\text{TS}} - T_{\text{TS}}}{T_{t,\text{SC}} - T_{\text{EC}}} \quad (25)$$

Assuming isentropic flow, the temperature, T_{EC} , can be calculated using the pressure measured at EC and the stagnation conditions of the tunnel as written in Eq. 26. This relation is equally applicable to conditions calculated at TS.

$$T_{\text{EC}} = T_{t,\text{SC}} \left(\frac{p_{\text{EC}}}{p_{t,\text{SC}}} \right)^{\frac{\gamma-1}{\gamma}} \quad (26)$$

After calibration, the velocity in the test section is solved for from the definition of the specific kinetic energy and Eq. 25, as shown in Eq. 27. The rest of the condition setting equations are shown in Eqs. 28 through 32.

$$V_{\text{TS}} = \sqrt{2 k_{\text{TS}}}, \quad \text{where } k_{\text{TS}} = C'_k c_p (T_{t,\text{SC}} - T_{\text{EC}}) \quad (27)$$

$$a_{\text{TS}}^2 = a_{t,\text{SC}}^2 - (\gamma - 1) k_{\text{TS}}, \quad \text{where } a_{t,\text{SC}}^2 = \gamma R T_{t,\text{SC}} \quad (28)$$

$$M_{\text{TS}} = V_{\text{TS}}/a_{\text{TS}} \quad (29)$$

$$p_{\text{TS}} = p_{t,\text{SC}} \left(1 + \frac{1}{2} (\gamma - 1) M_{\text{TS}}^2 \right)^{-\gamma/\gamma-1} \quad (30)$$

$$\rho_{\text{TS}} = \rho_{t,\text{SC}} \left(\frac{p_{t,\text{SC}}}{p_{\text{TS}}} \right)^{-1/\gamma}, \quad \text{where } \rho_{t,\text{SC}} = \frac{p_{t,\text{SC}}}{R T_{t,\text{SC}}} \quad (31)$$

$$q_{\text{TS}} = \rho_{\text{TS}} k_{\text{TS}} \quad (32)$$

III. The 14x22 Tunnel

A. Physical description

The 14x22 is a closed-circuit, continuous flow atmospheric tunnel. The test section can be set up in open, partially open, slotted or closed configurations. The test section is 50 ft long with a cross-sectional shape of approximately 14.5-ft high by 21.75-ft wide in the closed-throat configuration. The dynamic pressure can vary up to approximately 140 lbf/ft² depending on the test section geometry, and a Reynolds number up to 2.2 million per foot can be attained. The full tunnel circuit, shown in Fig. 2, is 770 feet long. The settling chamber starts around Sta. 700. The test section starts at Sta. 0 (coincident with Sta. 770). The diffuser extends from the end of the test section, Sta. 50, to the first corner at Sta. 192. Further details of the facility can be found in Applin [8] and Gentry [9].

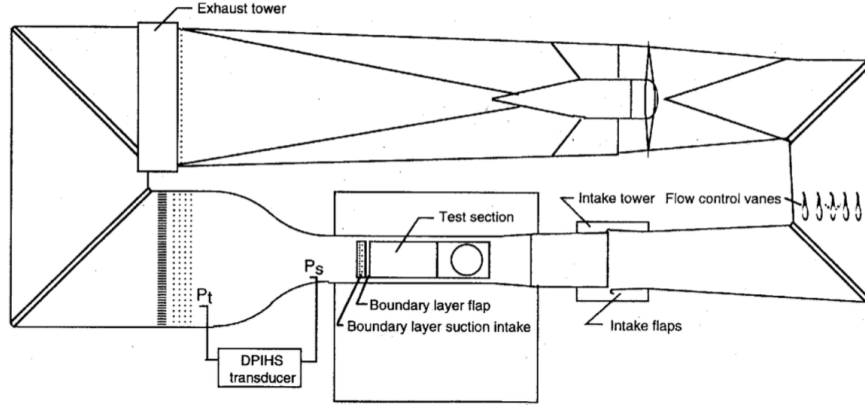


Fig. 2 Schematic of the 14x22 tunnel circuit, from Hallissy [10], Appendix B.

B. 14x22 Calibration Equation

The 14x22 wind tunnel uses the calibration equation following the incompressible methodology described in Sec. II.A. The nomenclature for the survey points as they apply to this facility are listed in Table 1. Figure 3 is a sketch of the tunnel showing the flow survey locations used in the 14x22. The calibration function, C' , is defined as the ratio of

Table 1 14x22 tunnel survey locations.

Parameter	Tunnel station	x (ft)
Settling chamber (SC)	711.	-56.3
Entrance cone (EC)	758.	-12.0
Test section (TS)	17.75	17.75

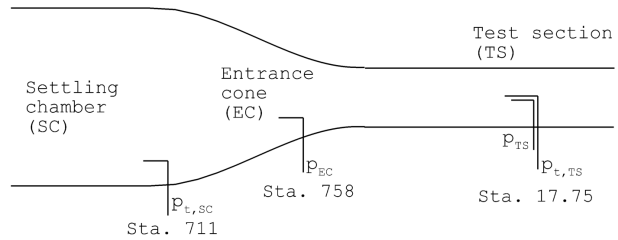


Fig. 3 Schematic of tunnel survey locations.

the incompressible dynamic pressure in the test section, $q_{i,TS}$, to the measured dynamic pressure upstream of the test section, $q_{i,indicated}$, shown in Eq. 33 (repeating Eq. 9). An extensive analysis of measurement errors associated with this equation can be found in Hensch [11].

$$C' = \frac{q_{i,TS}}{q_{i,indicated}} = \frac{P_{t,TS} - P_{TS}}{P_{t,SC} - P_{EC}} \quad (33)$$

C. 14x22 Condition Equations

Subsequent to the calibration process, the condition setting equations are used by the 14x22 tunnel to calculate representative values for parameters such as dynamic pressure, static pressure, and Mach number, for the flow in the test section. The equations used for calculating tunnel conditions are listed in Eqs. 34 through 41. The condition equations are based on the theory discussed in Sec. II.A with the addition of corrections due to water vapor content. [‡] In this section, the subscript ∞ is used to denote the state of the test section, with or without a test article present. It is assumed that the single probe measurements in the settling chamber and entrance cone, that are used for condition setting, are representative of the tunnel flow in those regions. In reality, there exists some degree of transverse variation of the tunnel flow that is not necessarily captured by these measurement probes, which could result in imprecise condition setting.

The tunnel condition equations were written for pressure in [lbf/ft²]; density in [slug/ft³]; temperature in degrees Rankine; the gas constant, 1716.2290 [ft²/s²- R]; velocity in [ft/s]; viscosity of air corrected for temperature in [slug/ft-s]; and unit Reynolds number in [1/ft]. In the CFD code FUN3D (described in Sec. IV.B), all nondimensional parameters that are solved for in the code are converted into Imperial units, where applicable, in order to compare with the results calculated using the facility equations.

The incompressible freestream dynamic pressure, $q_{i,\infty}$, is calculated by multiplying the incompressible dynamic pressure (or indicated pressure), $q_{i,indicated}$, and the calibration coefficient, C' , with a pitot-static probe recovery factor, K_{pr} , as shown in Eq. 34.

$$q_{i,\infty} = C' K_{pr} q_{i,indicated}, \quad \text{where} \quad q_{i,indicated} = P_{t,SC} - P_{EC} \quad (34)$$

The calibration equations for C' are shown in Fig. 4, next to the plot of C' against the indicated pressure. Other details of the calibration equations can be found in Quinto [12] and Boney [13].

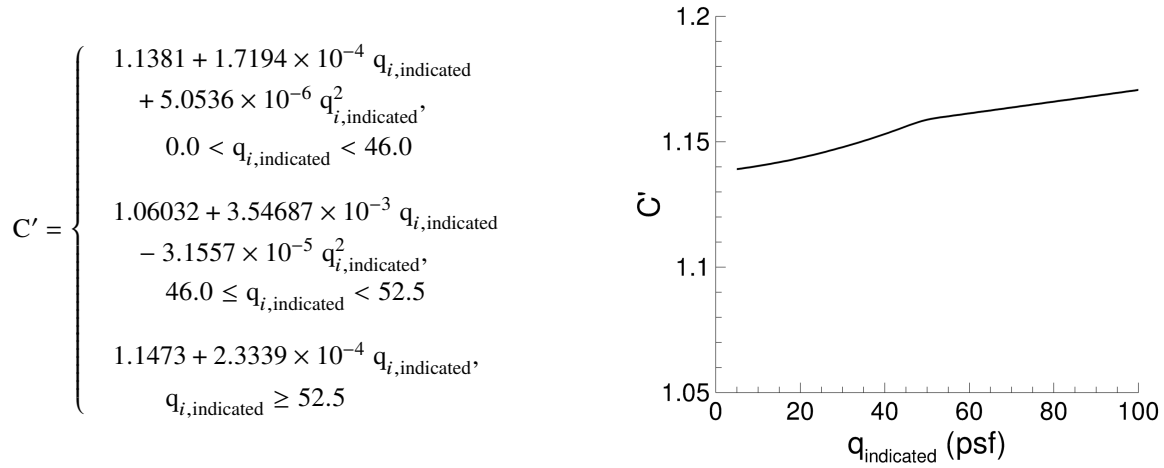


Fig. 4 14x22 facility calibration equation and curve, closed throat, no boundary layer suction.

The incompressible Bernoulli equation is used to calculate the freestream static pressure associated with the test section, p_∞ , shown in Eq. 35. A compressible freestream dynamic pressure, q_∞ , is calculated from the freestream Mach number, M_∞ , as shown in Eqs. 36 and 37.

$$P_\infty = P_{t,SC} - q_{i,\infty} \quad (35)$$

$$M_\infty = \sqrt{\frac{2}{\gamma - 1} \left[\left(\frac{P_{t,SC}}{P_\infty} \right)^{(\gamma-1)/\gamma} - 1 \right]} \quad (36)$$

$$q_\infty = \frac{1}{2} \gamma P_\infty M_\infty^2 \quad (37)$$

[‡]The presence of water vapor is not accounted for in the CFD.

The equations for vapor pressure, the corrected density, p_{vapor} , and compressible density, ρ_{∞} , are shown in Eqs. 38 and 39, respectively.

$$p_{\text{vapor}} = 12.7654 * \exp \left[\frac{((9.72334 T_{\text{dewpoint}}) - 311.147)}{((0.555556 T_{\text{dewpoint}}) + 223.192)} \right] \quad (38)$$

$$\rho_t = \frac{p_{t,SC} - 0.3789 p_{\text{vapor}}}{1716.2290 T_{t,SC}}, \quad \rho_{\infty} = \rho_t \left(\frac{p_{t,SC}}{p_{\infty}} \right)^{-1/\gamma} \quad (39)$$

The freestream velocity, V_{∞} , is then calculated from the compressible freestream dynamic pressure, q_{∞} , instead of the incompressible form, $q_{i,\infty}$, as listed in Eq. 40. The equations for unit Reynolds number and bulk viscosity are shown in Eq. 41. The temperature in the entrance cone, T_{EC} , used to calculate the bulk viscosity, is a measured parameter in the 14x22, rather than a calculated parameter seen previously in Eq. 26.

$$V_{\infty} = \sqrt{2 q_{\infty} / \rho_{\infty}} \quad (40)$$

$$\text{Re}_{L,\infty} = \frac{\rho_{\infty} V_{\infty}}{\mu_{\infty}}, \quad \mu_{\infty} = \frac{0.0002672}{T_{EC} + 198.72} \left(\frac{T_{EC}}{518.69} \right)^{3/2} \quad (41)$$

D. Tunnel computational models

The set of *a priori* grid presented in Rumsey et al. [3] were also utilized for the initial solution sensitivity study in this paper. A sketch of the outer shell of the high-speed leg is shown in Fig. 5a. The inflow boundary was at Sta. 700 ($x = -70$ ft.), just upstream of the screens, and a 92 foot extension, shown as the gray shaded portion of the tunnel in Fig. 5a, was added downstream of the actual tunnel diffuser that ended at Sta. 192. The extension was added to minimize the chance of reversed flow impinging the outflow boundary. The screens in the upstream portion of the settling chamber were not modeled in this study. Further details of these modeling choices are discussed in Ref. [3]. The area distribution of the tunnel circuit from tunnel Sta. 700 to Sta. 284 is plotted in Fig. 5b. A perspective view, looking downstream from the inflow boundary, showing the locations of the survey points used by both the physical tunnel and the CFD is presented in Figure 6. The computational simulations extracted the density, velocity and pressure in the settling chamber (SC), entrance cone (EC), and model center to calculate the total and static pressures at each location. In the 14x22 facility, pitot and static pressure tubes were used to measure the total pressure in the settling chamber (SC) and the static pressure in entrance cone (EC), respectively.

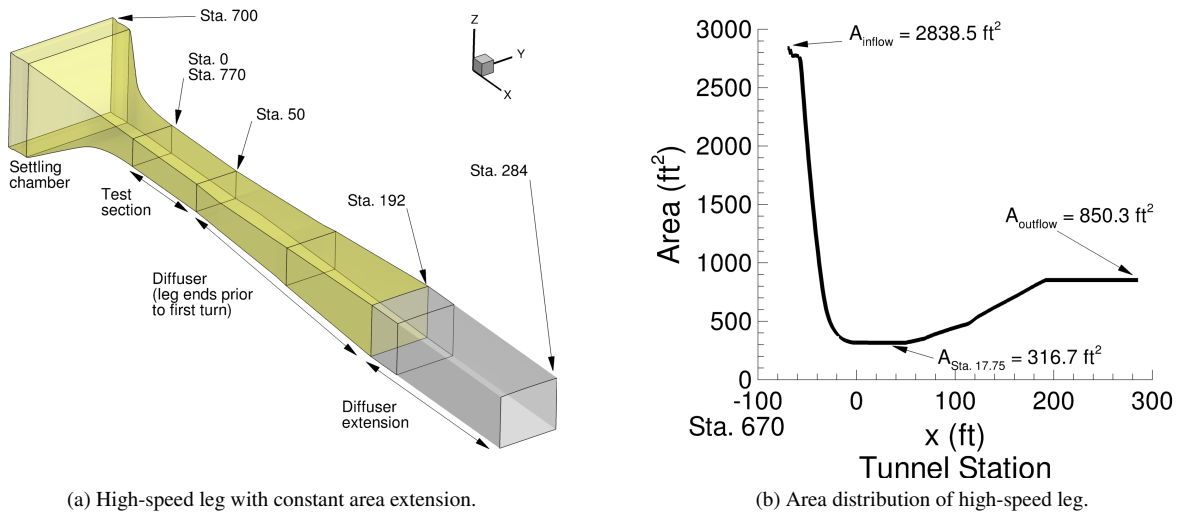


Fig. 5 Description of the computational model.

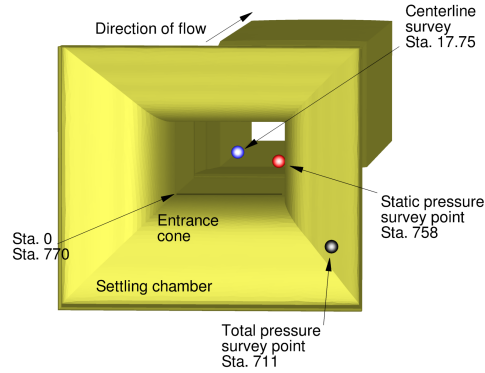


Fig. 6 Sketch of flow survey points, perspective view looking downstream from the settling chamber into the test section.

IV. Computational Methods

This section will present a brief overview of the one- and three-dimensional computational methods used in developing solutions for this study.

A. One-Dimensional Theory

The area distribution of the high-speed leg plotted in Fig. 5b can be used to generate a one-dimensional inviscid solution of the flow. Specifying the Mach number and cross-sectional area in the test section (minimum area), the Mach number at all other locations can be determined. A Newton's method can be used to solve the transcendental equation, Eq. 42, to determine the Mach number at any location in the tunnel, (see Ref. [14], Eq. 80).

$$M_{\text{local}} \left(1 + \frac{\gamma - 1}{2} M_{\text{local}}^2 \right)^{\frac{1}{2} - \frac{\gamma}{\gamma - 1}} = M_{\text{TS}} \left(\frac{A_{\text{TS}}}{A_{\text{local}}} \right) \left(1 + \frac{\gamma - 1}{2} M_{\text{TS}}^2 \right)^{\frac{1}{2} - \frac{\gamma}{\gamma - 1}} \quad (42)$$

B. FUN3D

FUN3D is an unstructured three-dimensional, implicit, Navier-Stokes code. Roe's flux difference splitting [15] is used for the calculation of the inviscid terms. In this work, the method for calculation of the Jacobian was the flux function of van Leer [16], and flux limiters were not used in any of the simulations. Solutions were developed using the SA-neg turbulence model with the QCR2020 Reynolds stress correction.[17]. Other details regarding FUN3D can be found in the manual [18], as well as in the extensive bibliography that is accessible at the FUN3D website [19].

V. Problem Characterization

A. Reference and Freestream Parameters

This section will discuss the use and setting of reference parameters for FUN3D and how they relate to freestream conditions. Using the ideal gas path in FUN3D, the user input of reference Mach number, M_{ref} , unit Reynolds number, Re_L , and reference temperature, \tilde{T}_{ref} , completely defines the dimensional reference parameters of bulk viscosity, speed of sound (sonic speed), velocity, density, and pressure. The subscript 'ref' denotes a reference quantity, a tilde '~' denotes a dimensional quantity, and the subscript '∞' denotes a freestream quantity. An exhaustive list of the variables used in the code are discussed in Sec. 2 of the FUN3D manual [18].

A comparison of several dimensional and equivalent nondimensional reference parameters used in the code are listed in Table 2. The reference temperature, reference density, reference speed of sound, and reference bulk viscosity are used to nondimensionalize parameters in the code. The nondimensional reference values for external flows are the

same for internal flows. The nondimensional reference values for temperature, density and the speed of sound are 1.0 in the ideal gas path. The nondimensional reference static pressure is a constant equal to $1/\gamma$.

Table 2 FUN3D reference parameters.

Parameter	Units	Dimensional	Non-dimensional (Compressible)
Sonic speed	m/s	$\tilde{c}_{\text{ref}} = \sqrt{\gamma R \tilde{T}_{\text{ref}}}$	$c_{\text{ref}} = 1$
Velocity	m/s	$\tilde{V}_{\text{ref}} = M_{\text{ref}} \tilde{c}_{\text{ref}}$	$V_{\text{ref}} = M_{\text{ref}}$
Density	kg/m ³	$\tilde{\rho}_{\text{ref}} = \text{Re}_L \tilde{\mu}_{\text{ref}} / \tilde{V}_{\text{ref}}$	$\rho_{\text{ref}} = 1$
Pressure	Pa	$\tilde{p}_{\text{ref}} = \tilde{\rho}_{\text{ref}} R \tilde{T}_{\text{ref}}$	$p_{\text{ref}} = \tilde{p}_{\text{ref}} / \tilde{\rho}_{\text{ref}} \tilde{c}_{\text{ref}}^2 = 1/\gamma$
Temperature	K	\tilde{T}_{ref}	$T_{\text{ref}} = 1$

B. External and Internal Flow Characterization

Whether a simulation is an external flow or an internal flow is largely dependent upon the boundary conditions of the numerical model. External flow simulations typically have a farfield region with no outer boundary constraint, other than setting the farfield Mach number to the reference Mach number. The conditions in the farfield are the same as the reference conditions, for example $M_{\infty} = M_{\text{ref}}$, $\tilde{p}_{\infty} = \tilde{p}_{\text{ref}}$, and $\tilde{T}_{\infty} = \tilde{T}_{\text{ref}}$. A common exception is when a simulation of a rotorcraft-in-hover uses rotor tip speed as the reference Mach number and the freestream Mach number is set to a different, usually smaller, value via the `vinf_ratio` parameter in the `&reference_physical_properties` namelist.

The concept of a farfield where the flow is considered fixed regardless of the aerodynamic problem being modeled does not exist for purely internal flow simulations. In this study, the concept of ‘freestream’ for the wind tunnel is defined as the current state of the flow in the test section. The goal is to set the outflow static pressure level such that the calculated Mach number for the test section, i.e., the freestream Mach number, is equal to the reference Mach number. If the freestream Mach number does not match the reference Mach number, the freestream static pressure in the test section will differ from the reference static pressure. The most noticeable consequence of a reference condition mismatch will be a shift in the pressure coefficients. The simulation is in the correct state when the conditions in the test section match the reference conditions of the problem. A comparison of freestream parameters is shown in Table 3.

Table 3 Comparison of External and Internal flow freestream parameters.

Parameter	External flow	Internal flow
c_{∞}	1	$\sqrt{T_{\infty} / T_{\text{ref}}}$
M_{∞}	M_{ref}	M_{∞}
ρ_{∞}	1	$\rho_{\infty} / \rho_{\text{ref}}$
p_{∞}	$1/\gamma$	$p_{\text{ref}} / (\gamma p_{\infty})$
$p_{t,\infty}$	$p_{\text{ref}} \left(1 + \frac{\gamma-1}{2} M_{\text{ref}}^2\right)^{\gamma/\gamma-1}$	$p_{\text{ref}} \left(1 + \frac{\gamma-1}{2} M_{\text{ref}}^2\right)^{\gamma/\gamma-1}$
T_{∞}	1	$T_{\infty} / T_{\text{ref}}$
$T_{t,\infty}$	$T_{\text{ref}} \left(1 + \frac{\gamma-1}{2} M_{\text{ref}}^2\right)$	$T_{\text{ref}} \left(1 + \frac{\gamma-1}{2} M_{\text{ref}}^2\right)$

C. Boundary conditions

There are several combinations of boundary conditions that can completely define an internal flow simulation. In this study, the specification of the total pressure, total temperature and velocity flow angle at the inflow boundary and static pressure at the outflow boundary was used. In the ideal gas path of FUN3D, the normalizations as discussed in

Stitt [20] were used; where the user inputs for those boundary conditions are divided by the reference static pressure and temperature, for pressure and temperature boundary conditions, respectively. Further details on the implementation boundary conditions in FUN3D can be found in Carlson [21].

1. Setting the inflow boundary conditions

Consider the simulation of the flow through a simple contraction section followed by a constant area test section as pictured in Fig. 7. Of specific interest is the Mach number, pressure, and temperature occurring in the test section of the wind tunnel. These quantities are primarily driven by the upstream inflow total conditions and the downstream outflow static pressure (back pressure) [22, 23]. There is a direct comparison with the freestream conditions of an external flow

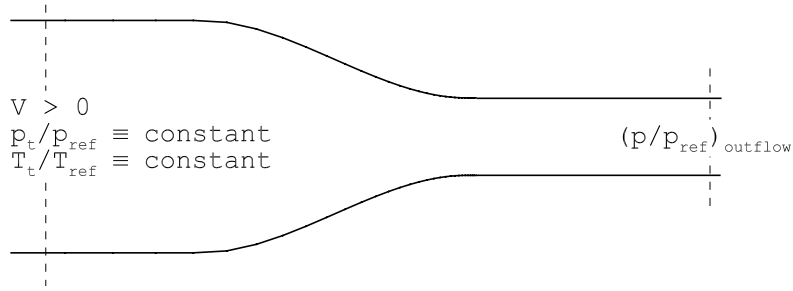


Fig. 7 Sketch of simple converging duct.

simulation when using the total conditions at the inflow boundary of an internal flow simulation as shown in Table 3. Though the Mach number in the test section can be increased or decreased somewhat arbitrarily as the static pressure imposed at the outflow boundary is decreased or increased, the proper value of the test section static pressure will only occur when the inflow boundary conditions are set using the isentropic relation with the reference Mach number; that is, Eqs. 43 and 44 and when the Mach number measured in the test section is equal to the reference Mach number. At these conditions, the local static pressure will then equal the reference static pressure, i.e., $p = p_{ref} = 1/\gamma$, and the pressure coefficient will be zero, $C_p = 0.$, see Eq. 45.

$$\frac{p_t}{p_{ref}} = \left(1 + \frac{\gamma - 1}{2} M_{ref}^2 \right)^{(\gamma/\gamma-1)} \quad (43)$$

$$\frac{T_t}{T_{ref}} = \left(1 + \frac{\gamma - 1}{2} M_{ref}^2 \right) \quad (44)$$

$$C_p = \frac{2}{\gamma M_{ref}^2} \left(\frac{p}{p_{ref}} - 1 \right) \quad (45)$$

2. Setting the outflow boundary condition

For inviscid flow simulations, the Mach number at the outflow boundary, M_{outflow} , can be calculated using Eq. 42 by replacing A_{local} with the outflow boundary area, A_{outflow} , and replacing M_{TS} with M_{ref} . The area ratio between the test section of the tunnel and the outflow area at the end of the computational tunnel diffuser, $A_{\text{TS}}/A_{\text{outflow}}$, will determine the static pressure at the outflow boundary. Newton's method is used to solve the transcendental equation for M_{outflow} . Assuming no total pressure loss in the tunnel, i.e., $p_{t,ts} = p_{t,\text{outflow}} = p_{t,\text{ref}}$, the static pressure ratio is then computed using Eq. 46.

$$p_{\text{back}} = \frac{\tilde{p}_{\text{outflow}}}{\tilde{p}_{\text{ref}}} = \frac{\tilde{p}_{\text{outflow}}/\tilde{p}_{t,\text{ref}}}{\tilde{p}_{\text{ref}}/\tilde{p}_{t,\text{ref}}} = \frac{\left(1 + \frac{\gamma-1}{2} M_{\text{outflow}}^2 \right)^{\frac{-\gamma}{\gamma-1}}}{\left(1 + \frac{\gamma-1}{2} M_{\text{ref}}^2 \right)^{\frac{-\gamma}{\gamma-1}}} \quad (46)$$

The inviscid value of p_{back} can be used as a starting point for viscous simulations. The degree of viscous loss is not known *a priori*, as discussed in the report by Rumsey et al. [3] and Rogers et al. [4], though, so p_{back} in the viscous flow case is somewhat lower than the pressure calculated for the inviscid flow case.

VI. Results and Discussions

This section starts with a discussion of the motivation to use CFD-based calibration curves, followed by computational results from the two calibration methodologies described in Sec. II. Centerline Mach and dynamic pressure distributions using the physical tunnel calibration curve and condition equations are discussed in Sec. VI.A. Section VI.B shows the calibration curves derived from a series of CFD simulations of the tunnel. Section VI.C examines the changes in the calibration curve due to a streamwise shift in the static pressure survey point in Sec. VI.C.

A. Using the 14x22 calibration curve in the CFD.

This section discusses solutions that were developed using the facility calibration curve shown in Fig. 4 for the condition $q_{\infty} = 60$ psf and $M_{\infty} = 0.20122$. The longitudinal (streamwise) centerline dynamic pressure and Mach number distributions are plotted in Figs. 8a and 8b. The model testing area extends from tunnel Sta. 5 to 30, as noted by the vertical bars in each plot. According to the 14x22 tunnel calibration curve, the dynamic pressure and Mach number should be at the levels of 60 psf and .20122, respectively. What is observed is that neither the dynamic pressure nor the concomitant Mach number distribution were within $\pm 0.5\%$ of the reference condition inside the bounds of the test section. At the location of the model center, Sta. 17.75, the dynamic pressure is about 1.5% low, and the Mach number is around .75% low.

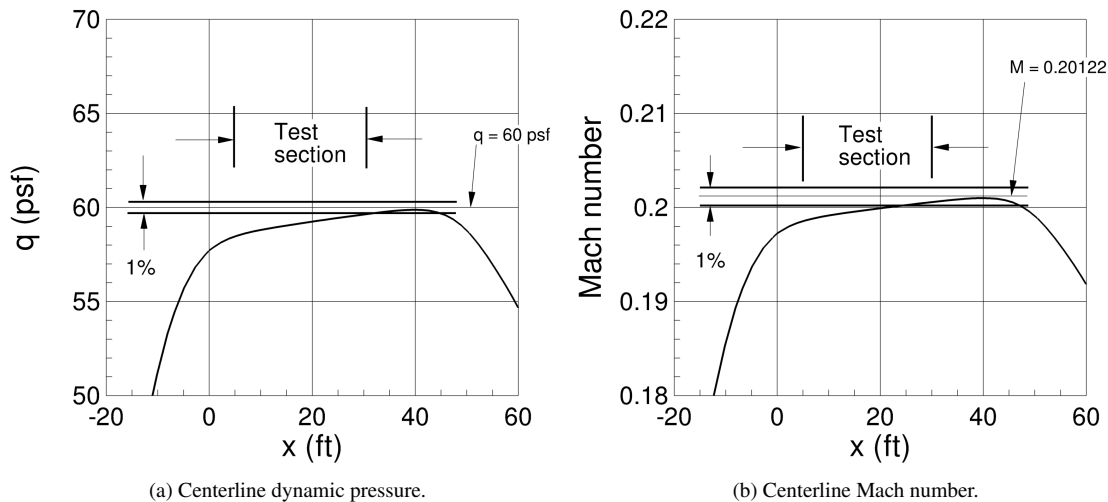


Fig. 8 CFD using 14x22 facility calibration curve, $q = 60$ psf, medium grid.

B. Calibration of the 14x22 using CFD

The calibration process using CFD parallels much of the process used by the facility: the indicated pressure, that is, the pressure difference between the settling chamber and the entrance cone, is measured for several tunnel flow conditions; the incompressible dynamic pressure of the test section flow is calculated; and a piecewise continuous calibration function of the incompressible dynamic pressure with the indicated pressure is created. Solutions were developed using the coarse, medium, and fine *a priori* grids at test section dynamic pressures of 20, 40, 60, 80, and 100 psf. The variation in streamwise incompressible dynamic pressure distributions along the tunnel centerline for a dynamic pressure of 60 psf is shown in Fig. 9. Solutions developed with the three grid levels predicted nearly identical pressure distributions. This comparison is not a grid convergence study because the boundary condition controller adjusted the back pressure slightly differently for each grid to achieve the requested condition in the tunnel test section.

Following the format of Gentry[9] (Fig. 16), the streamwise distributions for the range of tunnel conditions are shown in Fig. 10. Using Eq. 9 derived in Sec. II.A, and Eq. 25 in Sec. II.B, the calibration curves resulting from these CFD runs are plotted in Fig. 11 for the three grid density levels. The CFD calibration curves are relatively straight by comparison with the published 14x22 calibration curves; not displaying the change in slope and quadratic dependence with the indicated pressure, $p_{t,SC} - p_{EC}$, below 50 psf. The CFD calibration curves were closely grouped, varying less than 0.2% between grid density levels for the range of flow conditions. For this range of tunnel conditions, the incompressible and compressible theories produced essentially the same results. The maximum deviation of the CFD curve from the facility curve was approximately 2%. Predicting CFD calibration curves that are this close to the experimental data could indicate that modeling the high-speed leg with a uniform inflow captures at least the first order features of the test section flow.

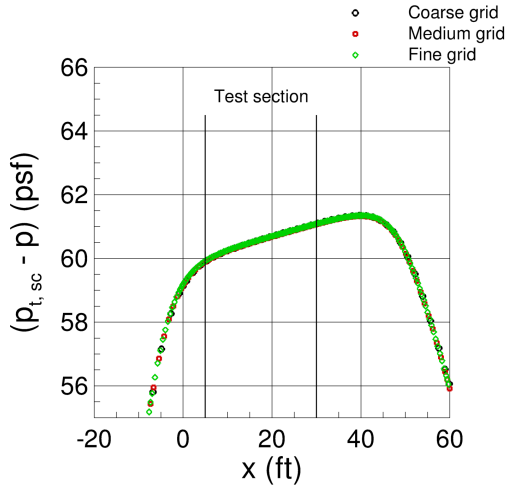


Fig. 9 Centerline incompressible dynamic pressures, *a priori* grid sensitivity, $Q = 60$ psf.

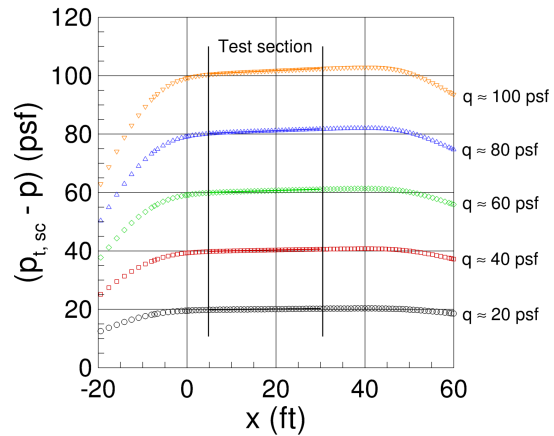


Fig. 10 Centerline incompressible dynamic pressures, *a priori* grid, medium density mesh.

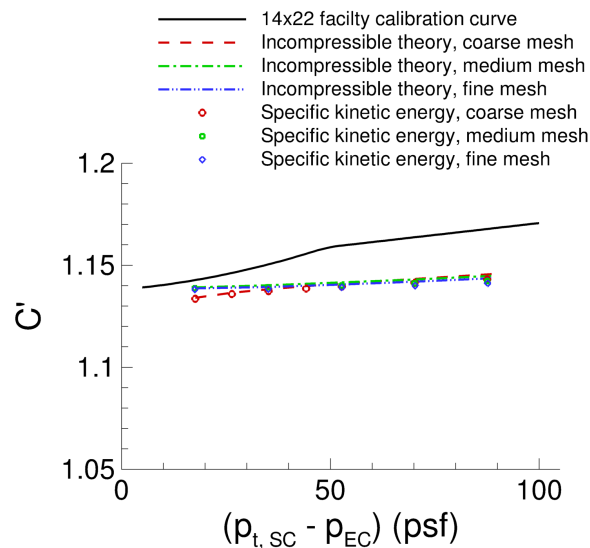


Fig. 11 Variation in calibration curves with grid density and thermodynamic theory, *a priori* grids.

C. Variation of calibration curves with entrance cone survey position

The variance of the C' function in the calibration equation, Eq. 47, with respect to the centerline pitot-static probe and the indicated pressure measurements, has been discussed in Hensch [11].

$$C' = \frac{P_{t,TS} - P_{TS}}{P_{t,SC} - P_{EC}} \quad (47)$$

The sensitivities of C' with respect to each of the pressures are given by Eq. 48.

$$\frac{\partial C'}{\partial P_{t,TS}} = \frac{1}{P_{t,SC} - P_{EC}}, \quad \frac{\partial C'}{\partial P_{TS}} = -\frac{1}{P_{t,SC} - P_{EC}}, \quad \frac{\partial C'}{\partial P_{t,SC}} = -\frac{C'}{P_{t,SC} - P_{EC}}, \quad \frac{\partial C'}{\partial P_{EC}} = \frac{C'}{P_{t,SC} - P_{EC}} \quad (48)$$

The check standard probe for measuring $p_{t,TS}$ and p_{TS} , and the pitot probe for measuring $p_{t,SC}$, are typically in regions of low streamwise pressure gradients and are also expected to be outside the influence of any boundary layer flows. In contrast, the flow passing by the static pressure probe in the entrance cone, p_{EC} , is rapidly accelerating as transits from the settling chamber into the test section. To examine the change of C' with respect to changes in the entrance cone survey location, the static pressure survey was translated upstream two feet and downstream two feet from the baseline survey location listed in Table 1. These locations, along with the current 14x22 survey point, are superimposed on the centerline pressure distribution plotted in Fig. 12. The pressure gradient varied from 1.63 psf/ft at the upstream survey point, $x = -14.0$ ft, to 0.59 psf/ft at the downstream survey point, $x = -10$ ft, giving a rate of change of the pressure gradient around 0.26 psf/ft/ft. At a dynamic pressure of 60 psf, the CFD predicts about a 2% shift above the 14x22 tunnel C' function using the upstream survey location and about a 6% shift below the 14x22 tunnel C' equation using the downstream survey location, as shown in Fig. 13. Even though the level of the predicted calibration curve is very sensitive to the location of the entrance cone static pressure survey location, the CFD solutions remain unchanged as long as the condition setting survey locations are consistent with the calibration survey locations.

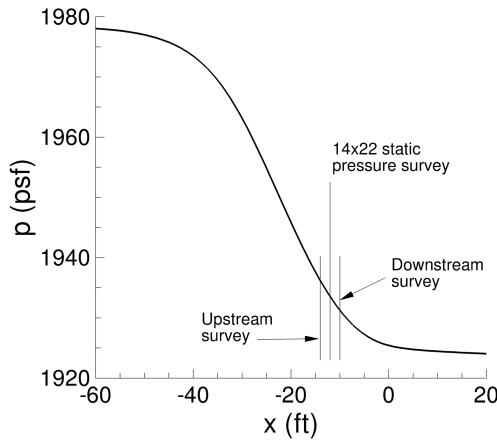


Fig. 12 Predicted pressure distribution through entrance cone with survey locations marked.

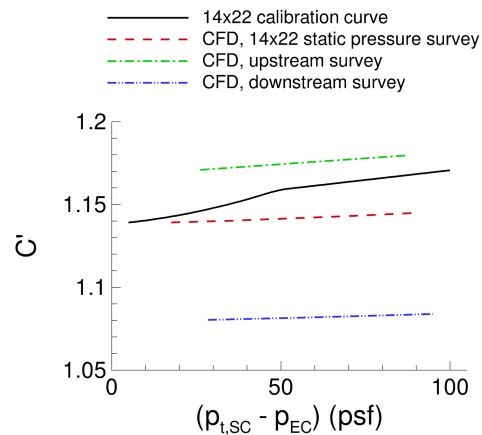


Fig. 13 CFD calibration curves due to streamwise variation of the static pressure survey location.

D. Verification of the 14x22 CFD condition setting

The previous sections discussed setting wind tunnel conditions using the 14x22 facility calibration curve, calibrating the tunnel using CFD, and the sensitivity of the calibration curve with respect to the location of the entrance cone pressure survey. This section will compare the output from the 14x22 tunnel data system with the output from the two condition setting methodologies using the respective CFD-based calibrations. Tunnel experimental condition data were extracted from three empty 14x22 runs at dynamic pressures of 40, 60, and 100 psf. For completeness, all three conditions are listed in Table 4. For brevity, only experimental parameters from the dynamic pressure of 100 psf are compared to empty tunnel computations in this discussion. Solutions were developed using the coarse, medium, and fine density sequence of hexahedral unstructured grids described in Sec. III.D. For each grid, the back pressure was adjusted

by the code to achieve a test section dynamic pressure of 100 psf. The settling chamber total pressure and entrance cone static pressure were measured and were used to calculate the tunnel conditions using both the incompressible and specific kinetic energy tunnel condition theories. Since the back pressure varied slightly grid-to-grid, the comparisons are not an indication of grid convergence, but are used for condition setting verification and sensitivity evaluation. A selection of parameters predicted by the two CFD condition setting methods are compared with the experimental data in Table 5. The dynamic pressure, Mach number, unit Reynolds number, velocity, and density in the test section were matched typically less than 0.1% when comparing between the 14x22 tunnel and all grid levels for each condition setting methods. Given the same tunnel parameter input, the output from the software for computing facility flow conditions and the CFD predictions closely agree. The following section will now revisit the simulation discussed in Sec. VI.A using the CFD-based calibration tools just discussed.

Table 4 Experimental data used for CFD calibration check points.^a

Run	Point	q_∞ (psf)	$Mach_\infty$	Re (1/ft)	T_t (°R)	V_∞ (ft/sec)	Δp^b (psf)	q_i^c (psf)	$P_{t,SC}/P_\infty^d$	ρ_∞ (slugs/ft ³)
136	638	40.003	0.1657	1.06226	555.3	191.86	35.048	40.28	1.01934	0.0021735
112	555	60.008	0.2038	1.28560	559.6	236.41	52.396	60.63	1.02937	0.0021474
133	623	100.004	0.2657	1.67384	552.5	305.60	87.340	101.78	1.05030	0.0021416

^a Tunnel data from Test 635.

^b Indicated differential pressure: $\Delta p_{i,indicated} = P_{t,SC} - P_{EC}$.

^c Incompressible dynamic pressure, see Eq. 35.

^d Ratio of stagnation pressure to test section static pressure used in Eq. 36.

Table 5 Calibration theory comparison with data, $q = 100$ psf.

Parameter	Tunnel Data ^a	Incompressible theory			Specific kinetic energy		
		Grid Density			Grid Density		
		Coarse	Medium	Fine	Coarse	Medium	Fine
Δp (psf) ^{b,e}	87.340	88.790	88.874	88.943	87.517	87.601	87.668
q_i (psf) ^c	101.78	101.78	101.80	101.77			
ρ_∞ (slugs/ft ³)	0.0021416	0.0021454	0.0021454	0.0021454	0.0021454	0.0021454	0.0021454
V_∞ (fps)	305.60	305.34	305.37	305.34	305.46	305.44	305.46
$P_{t,SC}/P_\infty^d$	1.05002	1.05003	1.05001	1.05002			
q_∞ (psf)	100.004	100.012	100.032	100.009	100.01	100.03	100.01
$Mach_\infty$	0.2657	0.2650	0.2650	0.2650	0.2650	0.2650	0.2650
Re (1/ft)	1.67384	1.67294	1.67311	1.67294	1.67294	1.67311	1.67294

^a Tunnel data from Test 635, Run 133, Point 623.

^b Indicated differential pressure using incompressible theory: $p_{t,SC} - p_{EC}$.

^c Incompressible dynamic pressure.

^d Ratio of stagnation pressure to test section static pressure used in Eq. 12.

^e Indicated differential pressure using specific kinetic energy: $\frac{\gamma}{\gamma-1} R \rho_{EC} (T_{t,SC} - T_{EC})$.

E. Evaluation of the CFD-based calibration curves

In this section, the results plotted in Fig. 8, are reexamined using the proposed CFD-based calibration and condition setting tools. New solutions were developed using the new calibration curve plotted in Fig. 11 with both of the incompressible and the specific kinetic energy condition setting equations that were discussed in Sec. II. The only

difference between the previous simulations and the revisited simulations is the calibration function used. All other code inputs were unchanged. Both theories yield the same results where the dynamic pressure and the concomitant Mach number distribution now match the reference conditions within the area of the test section, as shown in Fig. 14.

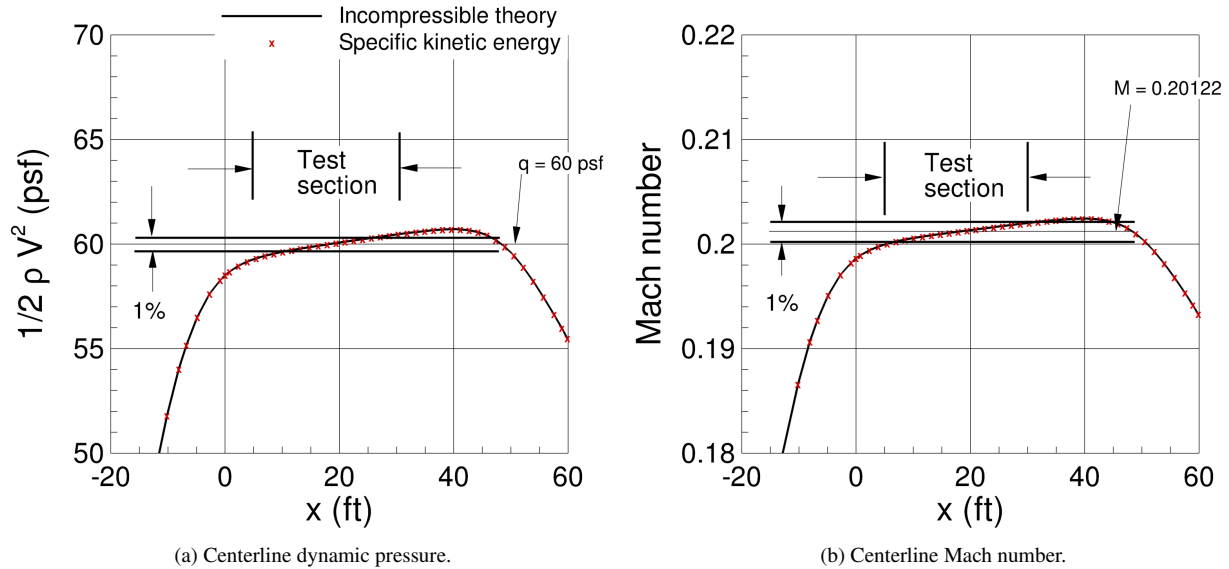


Fig. 14 CFD using CFD calibration curve, $q = 60$ psf, medium grid.

VII. Summary

The goals of this work were to better understand the calibration and condition setting process, to more accurately predict the flow in a wind tunnel test section, and to verify a more complete thermodynamic calibration and condition setting method. A brief review of the incompressible, pressure-based calibration theory historically used for closed-throat, subsonic tunnels was presented. To side-step the incompressible (isothermal) assumptions of the historical pressure-based calibration method, a compressible, enthalpy-based version calibration process was formulated and discussed. Calibration and condition setting simulations were performed using the 14x22 facility calibration and both the incompressible and the compressible methodologies. The effect of the entrance cone pressure survey location was also discussed. The calibration curves predicted by the computational method did not duplicate the shape nor match the level of the facility calibration curve. Simulations using the 14x22 facility calibration curve did not produce results that matched the requested test-section conditions. Tunnel simulations using the CFD-based calibrations were self-consistent and achieved the requested conditions in the test section. The incompressible, pressure and compressible, specific kinetic energy calibration and condition setting methodologies produced similar calibration curves and predicted nearly identical tunnel centerline dynamic pressure distributions.

Acknowledgments

This work was supported by the Transformational Tools and Technologies (TTT) Project of the NASA Transformative Aeronautics Concepts Program (TACP) and the Aerosciences Evaluation and Test Capabilities (AETC) Portfolio Office under the Aeronautics Research Mission Directorate.

References

- [1] Kegerise, M., and Neuhart, D. H., “Wind Tunnel Test of a Risk-Reduction Wing/Fuselage Model to Examine Juncture-Flow Phenomena,” NASA TM-2016-219348, NASA Langley Research Center, Nov. 2016.
- [2] Rumsey, C. L., and Morrison, J. H., “Goals and Status of the NASA Juncture Flow Experiment,” STO Applied Vehicle Technology (AVT) Panel, Progress and Challenges in Validation Testing for Computational Fluid Dynamics Paper Number AVT-246-03, Avila, Spain, Sep. 2016.
- [3] Rumsey, C. L., Carlson, J.-R., Hannon, J. A., Jenkins, L. N., Bartram, S. M., Pulliam, T. H., and Lee, H. C., “Boundary Condition Study for the Juncture Flow Experiment in the NASA Langley 14x22-Foot Subsonic Wind Tunnel,” AIAA Paper 2017-4126, Jun. 2017. doi:10.2514/6.2017-4126.
- [4] Rogers, S. E., Roth, K., and Nash, S. M., “CFD Validation of High-lift Flow with Significant Wind-tunnel Effects,” AIAA Paper 2000-4218, August 2000. doi:10.2514/6.2000-4218.
- [5] Carlson, J.-R., “Setting Boundary Conditions For Slotted Throat Wind Tunnels Using Calorically Imperfect Gas Assumptions,” AIAA Paper 2022-0807, Jan. 2022. doi:10.2514/6.2022-0807.
- [6] Carlson, J.-R., “Assessment of Using Ideal Gas for Predicting Boattail Flow at Cryogenic Temperatures,” AIAA Paper 2023-2275, Jan. 2023. doi:10.2514/6.2023-2275.
- [7] Pope, A., and Rae, W. H., *Low-Speed Wind Tunnel Testing*, 2nd ed., New York : Wiley, 1984.
- [8] Applin, Z. T., “Flow Improvements in the Circuit of the Langley 4- by 7-Meter Tunnel,” NASA TM-1983-85662, Dec. 1983.
- [9] Gentry Jr., C. L., Quinto, P. F., Gatlin, G. M., and Applin, Z. T., “The Langley 14- by 22-Foot Subsonic Tunnel: Description, Flow Characteristics, and Guide for Users,” NASA TP-3008, NASA Langley Research Center, Sep. 1990.
- [10] Hallissy, J. B., “14x22-ft Subsonic Tunnel Reference Condition Measurement Systems,” Internal facility document, Feb. 2008.
- [11] Hemsch, M. J., and Houlden, H. P., “Repeatability Modeling for Wind-Tunnel Measurements: Results for Three Langley Facilities,” AIAA Paper 2014-0096, 2014. doi:10.2514/6.2014-0096.
- [12] Quinto, P. F., and Boney, A. D., “Dynamic Pressure Equations Used at the Langley 14- by 22-Foot Subsonic Tunnel,” Technical Report L-32662, NASA Langley Research Center, May 2019. URL <http://hdl.handle.net/2060/20190018049>.
- [13] Boney, A. D., “Data Reduction Functions for the Langley 14- by 22-Foot Subsonic Tunnel,” NASA TM-2014-218513, NASA Langley Research Center, August 2014.
- [14] “Equations, Tables, and Charts for Compressible Flow,” NACA Rept. 1135, Jan. 1953.
- [15] Roe, P. L., “Approximate Riemann Solvers, Parameter Vectors, and Difference Schemes,” *J. Comp. Phys.*, Vol. 43, 1981, pp. 357–372. doi:10.1016/0021-9991(81)90128-5.
- [16] van Leer, B., “Towards the Ultimate Conservative Difference Schemes V. A second order sequel to Godunov’s Method,” *J. Comp. Phys.*, Vol. 32, 1979, pp. 101–136. doi:10.1016/0021-9991(79)90145-1.
- [17] Rumsey, C., Smith, B., and Huang, G., “Description of a Website Resource for Turbulence Model Verification and Validation,” AIAA Paper 2010-4742, June 2010. doi:10.2514/6.2010-4742, see also <http://turbmodels.larc.nasa.gov>.
- [18] Anderson, W. K., et al., “FUN3D Manual: 14.0.1,” NASA TM-2023-0004211, Apr. 2023.
- [19] <https://fun3d.larc.nasa.gov>, 2023. Accessed: 2023-04-11.
- [20] Stitt, L. E., “Exhaust Nozzle for Propulsion Systems With Emphasis on Supersonic Cruise Aircraft,” NASA RP-1990-1235, May 1990.
- [21] Carlson, J., “Inflow/Outflow Boundary Conditions with Application to FUN3D,” NASA TM-2011-217181, October 2011.
- [22] Jirasek, A., “Mass Flow Boundary Conditions for Subsonic Inflow and Outflow Boundary,” *AIAA Journal*, Vol. 44, No. 5, 2006, pp. 939–947.
- [23] Carlson, J.-R., “Automated Boundary Conditions for Wind Tunnel Simulations,” NASA TM-2018-219812, Mar. 2018.